Contents lists available at ScienceDirect

Applied Catalysis B: Environmental

Carbon gasification from Fe–Ni catalysts after methane dry reforming

Stavros Alexandros Theofanidis, Rakesh Batchu, Vladimir V. Galvita *, Hilde Poelman, Guy B. Marin

Laboratory for Chemical Technology, Ghent University, Technologiepark 914, B-9052 Ghent, Belgium

ABSTRACT

Carbon species removal was studied from a Fe–Ni catalyst supported on $MgAl_2O_4$ after methane dry reforming at 1023 K, atmospheric pressure and a CH_4/CO_2 molar ratio of 1:1. The deactivated and regenerated catalysts were characterized using X-ray photoelectron spectroscopy (XPS), Raman spectroscopy and energy-dispersive X-ray spectroscopy (EDX)-STEM mapping. The catalyst regeneration was studied by CO_2 and O_2 temperature programmed oxidation (TPO) and by operando time-resolved X-ray diffraction (XRD). A transient response technique, Temporal analysis of products (TAP), was applied to investigate the isothermal carbon species gasification.

Two different types of carbon species, graphitic and amorphous, were present after reaction. CO_2 oxidation could remove part of the carbon species, although EDX-STEM mapping showed the presence of carbon species located far from active metals phase even after CO_2–TPO at 1123 K. Carbon species removal by CO_2 involves two contributions: (1) the dissociation of CO_2 over Ni followed by the oxidation of carbon species by surface oxygen; (2) Fe oxidation by CO_2 and subsequent carbon species oxidation by Fe oxide lattice oxygen. The oxidation of carbon species by O_2 was identified from temperature programmed and isothermal experiments as a process including two processes: (1) oxidation of surface carbon by lattice oxygen and (2) particles migration to carbon species deposited far from active metals and subsequent oxidation through lattice oxygen of the iron and/or nickel oxides. The contribution of oxygen spillover in carbon gasification was considered to be negligible.

© 2015 Elsevier B.V. All rights reserved.

1. Introduction

Methane dry reforming (DRM) has been a subject of several studies for a long time [1]. The H_2/CO ratio from DRM is more favorable for Fischer-Tropsch and methanol synthesis than the ratio obtained from classical steam reforming [2]. Moreover, DRM has the lowest operating cost among these processes and offers the additional advantage of converting CO_2 into valuable chemicals:
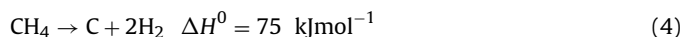
$$CH_4 + CO_2 \leftrightarrow 2CO + 2H_2 \quad \Delta H^0 = 261 \text{ kJ mol}^{-1} \quad (1)$$
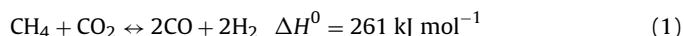
Side reactions of importance include the reverse water gas shift:

$$H_2 + CO_2 \leftrightarrow H_2O + CO \quad \Delta H^0 = 41 \text{ kJ mol}^{-1} \quad (2)$$
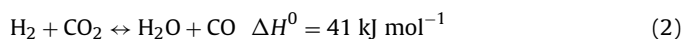
However, dry reforming technologies have the inherent disadvantage of rapid catalyst deactivation due to carbon deposition, i.e., coke [3]. Carbon deposition can originate either from the methane

decomposition reaction (Eq. (4)) or from CO disproportionation [4] (Eq. (3)):

$$2CO \leftrightarrow C + CO_2 \quad \Delta H^0 = -172 \text{ kJmol}^{-1} \quad (3)$$

$$CH_4 \rightarrow C + 2H_2 \quad \Delta H^0 = 75 \text{ kJmol}^{-1} \quad (4)$$

Carbon formation on metals from hydrocarbons decomposition is a complex process which includes surface catalysis and solid state reactions. Lobo and Trimm in 1971 [5–7] suggested a mechanism for steady-state carbon deposition on Ni catalysts. They suggested that the carbon atoms migrate through the Ni surface, upon which the hydrocarbon decomposition takes place, towards the active growth regions (carbides) where the process of carbon growth (nucleation) takes place [6]. The carbide phase decomposes at some stage to give graphite. Molecular mass and chemical structure of these carbon species may vary depending on the reaction type, conditions and catalyst [3,8,9]. Similarly, the carbon species deposited during DRM vary in morphology and may be carbidic, amorphous, graphene-like, graphitic, filamentous [4,10–13].

Several ways have been examined in order to inhibit or control the deactivation originating from carbon species deposition. Higher dispersion of the active metals on the support surface [14],

* Corresponding author. Fax: +32 93311759.
E-mail address: Vladimir.Galvita@UGent.be (V.V. Galvita).

increase of catalyst basicity to achieve a higher activation rate of mildly acidic CO_2 [15,16] and addition of materials that offer an oxygen reservoir through their redox behavior [17–20] have been investigated. Sadykov et al. [21] used CeO_2 as an oxygen reservoir material for DRM and showed that the oxygen mobility of CeO_2 can be increased by incorporation of rare earth metals (La, Gd and Pr) as dopants. They found that catalytic activity is correlated with oxygen near the surface and/or bulk mobility for elimination of deposited carbon species. Theofanidis et al. [22] on the other hand used Fe_2O_3 as promoter for a $Ni/MgAl_2O_4$ catalyst because of its good redox properties [23]. They found lower amounts of deposited carbon after methane dry reforming on Fe-modified samples in comparison with pure $Ni/MgAl_2O_4$. This was attributed to FeO_x formation during DRM reaction and subsequent oxidation of carbon by lattice oxygen [24–26]. Zhang and Verykios [16] showed that Ni/La_2O_3 activity increases after 2–5 h time-on-stream (TOS). This study revealed a CO_2 pool, stored in the form of $La_2O_2CO_3$.

However, despite all the different ways to reduce carbon deposition, carbon accumulation during reforming reactions remains an issue. Eventually, catalyst regeneration is required, by removing all carbon species by gasification [27,28]. There are many reports in literature proposing different mechanisms for catalytic carbon gasification. Some of the mechanisms that are mentioned are: (1) carbon bulk diffusion, where carbon is transported through the metal particle to the region where the gasification reaction takes place [6,29,30], (2) oxygen spillover where metal-activated oxygen may migrate over a considerable distance over the support towards the deposited carbon species and oxidizing them [31,32] and (3) the redox mechanism, where the catalyst provides oxygen towards carbon (reduction step) and is itself oxidized by the gas phase (oxidation step) [33–35]. Figueiredo and Trimm in 1975 [29] studied the gasification of carbon deposits on Ni foil and supported Ni catalysts. They found a zero reaction order for carbon gasification by steam, concluding that the reaction is controlled by the diffusion of carbon through Ni. Machida et al. [36] used CeO_2 as an active catalyst for soot oxidation concluding to two possible reaction pathways: (i) soot oxidation by adsorbed superoxide species (O_2^-) at the three-phase boundary (catalyst, carbon and gas) and (ii) soot oxidation by active lattice oxygen at the CeO_2/soot interface.

The rate of gasification depends on the structure of the carbon [37], its location [11] and on the nature of the catalysts present [10,38,39]. One important method for carbon species characterization is temperature programmed (TP) techniques [40,41]. However, isothermal studies are also required in order to understand the kinetics [28]. Oxygen is one of the gases most often used [42] to infer type and location of carbon species on the catalyst while there are also studies on carbon gasification by CO_2, H_2O and H_2 [4,29,31,43]. Among the latter, the mechanism according to which carbon species are oxidized by CO_2, as well as, the differences between CO_2 and O_2 carbon species removal await clarification. In view of the promising results on $Fe–Ni/MgAl_2O_4$ [22] regarding reduced carbon species deposition, this material was used for further investigation of carbon removal. The questions raised are addressed by performing X-ray diffraction (XRD) characterization of used $Fe–Ni/MgAl_2O_4$ catalysts, both in situ during O_2 temperature-programmed oxidation (TPO), as well as operando by coupling in situ XRD with MS. Further, for first time to our knowledge a transient response technique, Temporal Analysis of Products (TAP), has been used to investigate the isothermal carbon species gasification process. The latter is recognized as an important experimental method for heterogeneous catalytic reaction studies. A TAP pulse response experiment consists of injecting a very small amount of gas, typically nanomoles per pulse, into a tubular fixed bed reactor that is kept under vacuum. The time-dependent exit flow rate of each gas is detected by a mass spectrometer. The high time resolution of the TAP technique allows detection of short-(millisecond time scale) and/or long-lived (>1 s) reaction intermediates, which helps to formulate the mechanism of reaction [44,45].

2. Experimental methods

2.1. Catalyst preparation

2.1.1. Support preparation

The support material of $MgAl_2O_4$ was prepared by co-precipitation from an aqueous solution of $Mg(NO_3)_2\cdot 6H_2O$ (99%, Sigma–Aldrich) and $Al(NO_3)_3\cdot 9H_2O$ (98.5%, Sigma–Aldrich) (molar ratio Mg:Al = 1:2). A precipitating agent, NH_4OH (ACS reagent, 28.0–30.0% NH_3 basis) was added to adjust the pH to 10, at 333 K. The formed precipitate was filtered, dried at 393 K for 12 h and finally calcined in air at 1023 K for 4 h.

2.1.2. Catalyst preparation

8 wt% Ni-5 wt% Fe (named as "as-prepared Fe–Ni") was prepared by incipient wetness impregnation on the support ($MgAl_2O_4$) using an aqueous solution of corresponding nitrates $Ni(NO_3)_2\cdot 6H_2O$ (99.99 + %, Sigma–Aldrich) and $Fe(NO_3)_3\cdot 9H_2O$ (99.99 + %, Sigma–Aldrich) [46]. The catalysts were dried at 393 K for 12 h and subsequently calcined in air at 1023 K for 4 h.

2.2. Catalyst characterization

The BET surface area of the catalyst was $84.7 \pm 5.8\,m^2/g_{cat}$. A more detailed characterization of the catalyst has been reported elsewhere [22]. The crystallographic phases of the materials were confirmed by ex-situ XRD measurements (Siemens Diffractometer Kristalloflex D5000, Cu $K\alpha$ radiation). The powder patterns were collected in a 2θ range from $10°$ to $80°$ with a step of $0.02°$ and 30 s counting time per angle. XRD patterns of known compounds are referenced by their corresponding number in the powder diffraction file database.

High-resolution transmission electron microscopy (HRTEM) was used for structural analysis, while EDX yielded local chemical analysis. These techniques were implemented using a JEOL JEM-2200FS, Cs-corrected microscope operated at 200 kV, which was equipped with a Schottky-type field-emission gun (FEG) and EDX JEOL JED-2300D. All samples were deposited by immersion onto a lacey carbon film on a copper support grid.

XPS measurements were recorded with a S-Probe XPS spectrometer (VG, Surface Science Instruments), equipped with a monochromatized 450W Al $K\alpha$ source. The base pressure of the analysis chamber was below 2×10^{-7} Pa. Spectra were recorded with 200W source power. The analyzer axis made an angle of $45°$ with the specimen surface. Wide scan spectra were measured with a pass energy of 157 eV and a 0.2 eV step, while core levels were recorded with a step of 0.05 eV and a pass energy of 107.8 eV. Energy calibration to Al2p or C1s gave the same result, so the main intensity of C1s at 284.6 eV was used for alignment.

Raman analysis of the samples was performed on a RXN1 Raman spectrometer (Kaiser Optical Systems) fitted with a 532 nm laser operating at 40 mW.

2.3. Ageing of catalyst during DRM

The ageing of the catalyst was performed at atmospheric pressure in a quartz reactor with an internal diameter of 10 mm, which was housed inside an electric furnace. The temperature of the catalyst bed was measured with K-type thermocouples touching the outside and inside of the reactor at the position of the catalyst bed. The inlet gas flow rates were always maintained by means of
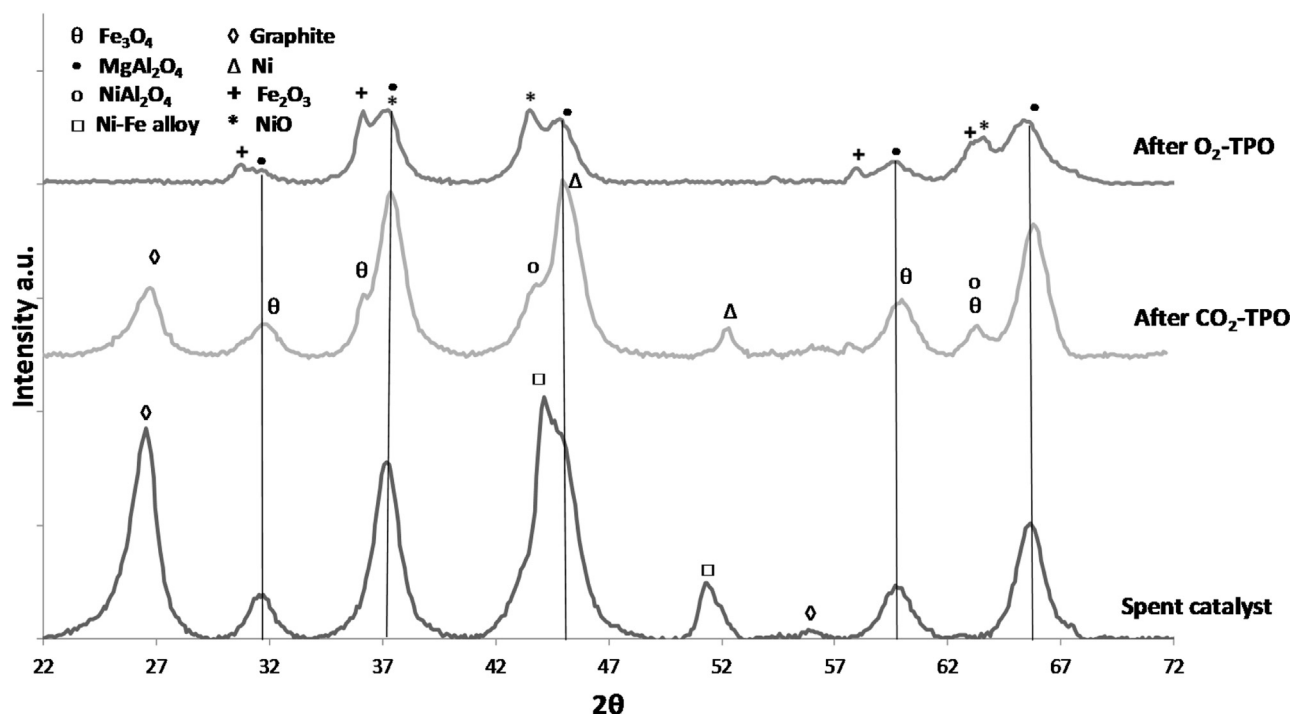
Fig. 1. Full XRD scans of used Fe–Ni (DRM for 1 h, 1023 K, $CH_4/CO_2/He = 1.1/1/1$, total pressure of 101.3 kPa), after CO_2–TPO (maximum temperature 1123 K, flow rate 10 ml/s) and after O_2–TPO (maximum temperature 1123 K, flow rate 10 ml/s).

calibrated Bronkhorst mass flow controllers. Prior to each experiment, the fresh sample was reduced in a 1 ml/s flow of 10% H_2/He at 1123 K for 30 min and then the flow was switched to He for 10 min. Based on previous experiments, this treatment allowed to fully reduce the material [22]. 70 mg of sample with particle size of ~30 μm, diluted with inert Al_2O_3 for improved heat conductivity (ratio catalyst/inert = 1/40), was packed between quartz wool plugs resulting in approximately 1.3×10^{-2} m of catalyst bed length. Control characterization experiments were performed on this material (referred to as "reduced Fe–Ni"). After this step a mixture of CH_4, CO_2 and He (total flow of 80 ml/min, volumetric ratio $CH_4/CO_2/He = 1.1/1/1$, He internal standard) started flowing through the reactor for carbon species deposition on the catalyst during DRM reaction at 1023 K and atmospheric pressure for 1 h, yielding a "used Fe–Ni catalyst". Produced CO, H_2 and unconverted CH_4 and CO_2 were detected at the outlet using a calibrated OmniStar Pfeiffer mass spectrometer (MS). MS signals were recorded for all major fragments. For quantification of reagents and products, the MS was focused to different amu signals. H_2 was monitored at 2, He at 4, CH_4 at 16, H_2O at 18, CO at 28, Ar at 40 and CO_2 at 44 amu. A correction was applied to remove contributions from unavoidable interference with fragmentation peaks of other gases.

The absence of external and internal mass transfer limitations was verified using the Carberry number [47] and Weisz-Prater criterion [48], while for heat transport limitations the diagnostic criteria reported by Mears [49] were applied.

2.4. Carbon species temperature programmed oxidation (TPO)

The TPO measurements were performed subsequent to the ageing experiment at atmospheric pressure after cooling down to room temperature. In a typical TPO experiment, the used catalyst was heated from ambient temperature to 1123 K under CO_2 or 10% O_2/He stream. The heating rate used for CO_2– and O_2–TPO was 10 K/min and the total gas flow rate was 1 ml/s. The TPO experiment was performed over the used Fe–Ni catalyst as

well as over Ni/MgAl$_2$O$_4$ (named "Ni") and commercial graphite (Sigma–Aldrich, powder, <20 μm), as reference materials for comparison purposes.

2.5. Operando XRD

The evolution of the structure during CO_2–TPO was investigated with time-resolved XRD. In situ XRD measurements were performed in a reactor inside a Bruker-AXS D8 Discover apparatus (Cu Kα radiation of 0.154 nm). The reactor had a Kapton foil window for X-ray transmission. The setup was equipped with a linear detector covering a range of 20° in 2θ with an angular resolution of 0.1°. The pattern acquisition time was 10 s. All temperatures were measured with a K-type thermocouple and corrected afterwards to a calibration curve of the heating device, which is based on the eutectic systems Au–Si, Al–Si and Ag–Si. For each sample, approximately 10 mg of powdered sample was evenly spread on a single crystal Si wafer. Interaction of the catalyst material with the Si wafer was never observed. Gases were supplied to the reactor chamber with calibrated mass-flow controllers. The sample was heated from room temperature to 1123 K at a heating rate of 20 K/min in a flowing gas stream (10 ml/s of CO_2 or 10% O_2/He). The outlet gas stream (CO, CO_2 and He) was monitored online using a calibrated OmniStar Pfeiffer mass spectrometer (MS).

A full XRD scan (10–65° with step of 0.02°) was taken at room temperature before and after the TPO experiment. Samples were cooled in helium flow to room temperature after each experiment.

2.6. Isothermal Temporal Analysis of Products (TAP) experiments for carbon gasification

Transient measurements were performed in a TAP-3E reactor (Mithra Technologies, St. Louis, USA) equipped with an Extrel Quadrupole Mass Spectrometer (QMS). The details of TAP experiments, can be found in [44]. For the experiments, 20 mg (250 < d < 500 μm catalyst fraction) of the calcined catalyst was
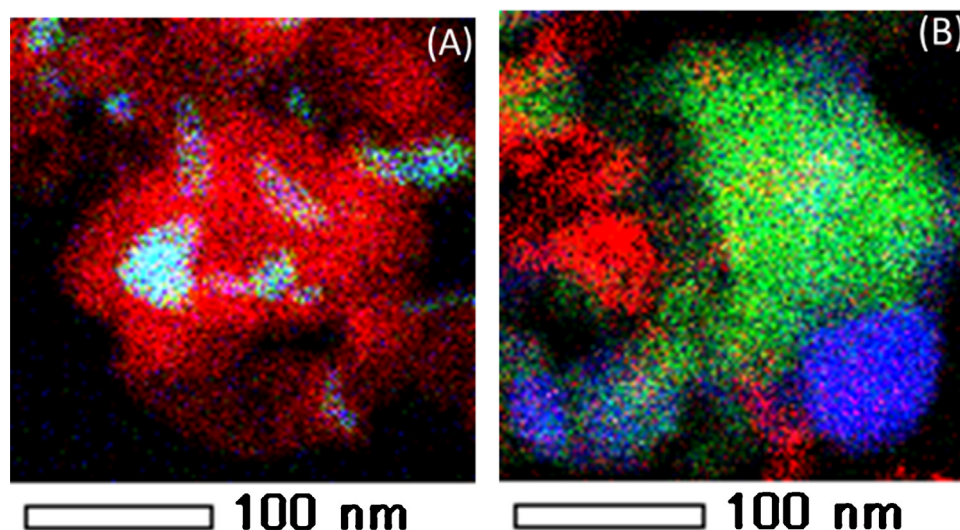
Fig. 2. EDX element mapping of Fe–Ni. (A) after DRM (1023 K, $CH_4/CO_2/He = 1.1/1/1$, total pressure of 101.3 kPa, reaction time 1 h). (B) after CO_2 oxidation (1 ml/s of CO_2 at a total pressure of 101.3 kPa and 1123 K). Red, green and blue colors correspond to carbon, Fe and Ni elements respectively. (For interpretation of the references to color in this figure legend, the reader is referred to the web version of this article.)

placed in a quartz microreactor (I.D = 4 mm and ∼2 mm bed length), which was located between two inert beds of quartz particles with the same sieved fraction. The temperature of the catalyst was measured by a K-type thermocouple housed inside the catalytic zone. Prior to the experiments, the catalyst was reduced at 1023 K in a flow of 10% H_2/He at atmospheric pressure. A series of CH_4 pulses (∼10^{-7} mol/pulse) were used isothermally for carbon deposition on the catalyst, yielding an "aged Fe–Ni catalyst", and the amu signals of 2 and 16 were monitored by QMS. For every 1 s, data were recorded with millisecond time resolution in each pulse.

A sequence of isothermal O_2 or CO_2 pulses were admitted into the microreactor for carbon gasification and CO_2, CO responses were monitored at amu signals of 44 and 28, respectively. The latter were recorded with millisecond time scale resolution for 20 s collection time. The burn-off sequence continued until the completion of carbon gasification with CO_2 and CO intensity responses equal to zero.

3. Results and discussion

3.1. Catalyst characterization

The crystalline phases of the Fe–Ni catalyst after DRM and after CO_2–TPO for carbon species removal are presented in Fig. 1. Identification of the XRD patterns is performed using the invariable peaks of the support as standard and interpreting the remainder diffractions in terms of position and relative intensity. The used catalyst shows peaks of $MgAl_2O_4$ (31.7°, 37°, 45°, 55.5°, 59°, 65°, powder diffraction file (PDF) card number: 00-021-1152), Fe–Ni alloy peaks (44° and 51.5°, PDF card number: 00-038-0419) and graphite diffraction peaks (26.6°, 43.4°, 46.3°, 56.7° PDF card number: 01-075-2078). Nickel or iron carbide diffraction peaks were not detected. The XRD pattern following the CO_2–TPO shows that the Fe–Ni alloy was decomposed to Ni (44.5° and 51.8°) and Fe_3O_4 (30.1°, 36°, 43.5°, 57°, 63°). The $NiAl_2O_4$ crystalline phase that was present in the reduced sample (not shown) [22] disappeared after DRM but a small diffraction peak appeared after CO_2 oxidation. $MgAl_2O_4$ diffraction peaks remained stable after CO_2-oxidation at 1123 K while the graphite peak was still present but with reduced intensity. This implies that the carbon species cannot be completely removed by CO_2. The XRD pattern after O_2–TPO showed that the graphite peak completely disappeared and that the catalyst struc-

ture was now similar to the structure of the fresh catalyst with separate Fe_2O_3 (maghemite) and NiO supported on $MgAl_2O_4$.

The elemental distribution of Fe–Ni is indicated in Fig. 2 using energy-dispersive X-ray spectroscopy (EDX)-STEM mapping. Carbon species (red) cover the Ni (blue) and Fe (green) particles that are in alloy formation (light blue) after DRM (Fig. 2(A)). In contrast, after CO_2 oxidation Ni and Fe particles are segregated as Fe is oxidized to Fe_3O_4 and the Fe–Ni alloy is decomposed. As it is reported elsewhere [22] a subsequent H_2 reduction step can lead again to Fe–Ni alloy formation restoring the initial activity.

Furthermore, it is observed that the carbon species in contact with the active metal phase are mainly removed. Fig. 2(B) shows that after CO_2 oxidation there are carbon species located at a distance from Ni and Fe. This implies that gas phase CO_2 does not interact directly with the deposited carbon species, up to 1123 K.

3.2. Carbon species temperature programmed oxidation

CO_2– and O_2–TPO profiles are presented in Fig. 3 comparing used Fe–Ni with the reference materials of Ni/$MgAl_2O_4$ and graphite, for the same heating rate of 10 K/min. Carbon oxides intensities as a function of temperature are illustrated. The CO signal for the used Ni sample (Fig. 3(A)) showed one maximum at 890 K and no multiple-peak profile. However, one maximum at 1020 K and one shoulder at 890 K were observed during CO_2–TPO over used Fe–Ni. The shoulder at lower temperature can be attributed to carbon species oxidation by Ni surface oxygen, originated from CO_2 dissociation, as it coincides with the peak maximum of the TPO profile obtained over used Ni. Metallic Ni remains stable under CO_2 and is not oxidized to NiO up to 1123 K [22,23]. Furthermore, the main peak maximum for used Fe–Ni can be assigned to carbon species oxidation by Fe oxide. This implies that the mechanism of carbon species removal over Ni is different from that over Fe–Ni catalyst. Pure graphite was also investigated during CO_2–TPO but no produced CO was detected up to 1173 K.

Fig. 3(B) displays the CO_2 intensity upon O_2–TPO with respect to temperature for used Ni, Fe–Ni and pure graphite. The deposited carbon species can either be oxidized by lattice oxygen, by surface oxygen originated from O_2 dissociation or by direct interaction with gas phase O_2. The CO_2 signal now showed one maximum for the studied samples. However, the peak maximum obtained by oxidation of carbon species over Ni and Fe–Ni is shifted to
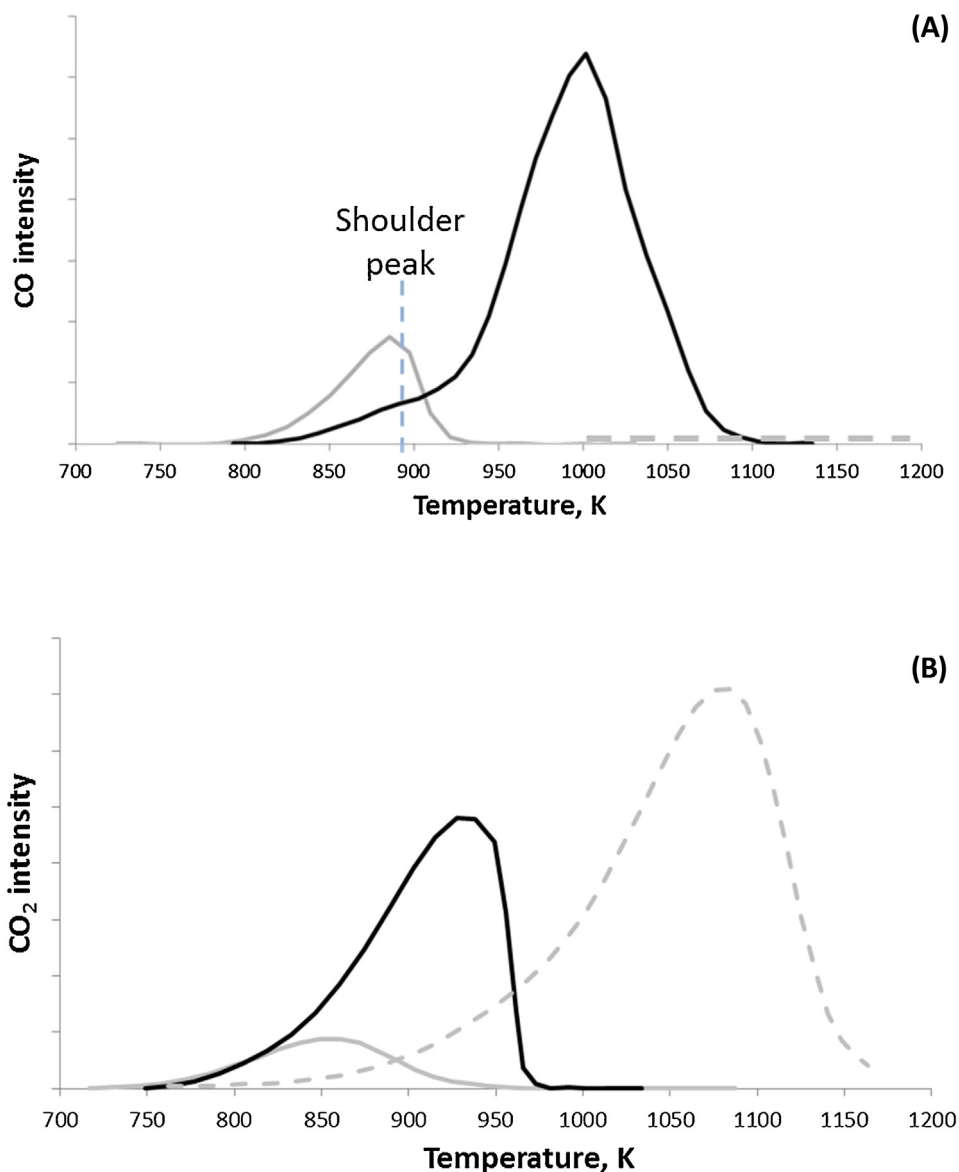
Fig. 3. (A) CO_2–TPO profile: CO intensity as a function of temperature for used (DRM for 1 h, 1023 K, $CH_4/CO_2/He = 1.1/1/1$, total pressure of 101.3 kPa) Ni, Fe–Ni and graphite heating rate of 10 K/min, flow rate of 1 ml/s of CO_2. (B) O_2–TPO profile: CO_2 intensity as a function of temperature for used Ni, Fe–Ni and graphite, heating rate of 10 K/min, flow rate of 1 ml/s of 10% O_2/He. Black line: Fe–Ni, grey line: Ni and dashed line: graphite.

lower temperatures than that of pure graphite oxidation, implying that the deposited carbon species are mainly oxidized by lattice or surface oxygen. However, as the temperature increases, direct interaction of carbon species with gas phase O_2 also takes place, contributing to the gasification process. The lower peak maximum of 850 K for Ni vs 920 K for Fe–Ni, implies that the carbon removal mechanism is somewhat different over both samples.

Fig. 3 shows that a higher amount of carbon was deposited on Fe–Ni than on the Ni catalyst. This is attributed to the CH_4-rich environment in which DRM takes place during catalyst ageing (volumetric $CH_4/CO_2/He = 1.1/1/1$). Bimetallic catalysts are more active for methane decomposition reaction than monometallic catalysts [50,51]. Theofanidis et al. [22] showed that during DRM with $CH_4/CO_2 = 1/1$, Fe addition suppresses carbon deposition on Ni as oxygen from the FeO_x lattice is transferred to nearby Ni atom, producing CO.

3.3. Carbon characterization

Raman spectroscopy is widely used in order to investigate the structure and the crystallite size of carbon species [52]. It provides information about the electronic properties and can detect the presence of ordered carbon species [4]. The Raman spectrum of a single crystal graphene sample only shows the G band at approximately 1581 cm^{-1} Raman shift. The commercial graphite, that was used as a reference, shows two peaks at 1555 and 1580 cm^{-1} Raman shift (blue line in Fig. 4). However, in case of imperfect, polycrystalline graphite and other carbonaceous materials [53], additional bands are detected at 1355 cm^{-1} (D band) and 1620 cm^{-1} (D′ band). The ratio of areas I_D/I_G has been correlated to the inverse crystallite size of graphite [54]. Fig. 4 shows the Raman spectra for the graphite, the used Fe–Ni catalyst after 1 h TOS during DRM at 1023 K, the used Fe–Ni catalyst after CO_2–TPO to 950 K (removal of shoulder peak on Fig. 3A) and the used Fe–Ni catalyst after CO_2–TPO to 1123 K. The analysis of used Fe–Ni (black line in Fig. 4) con-
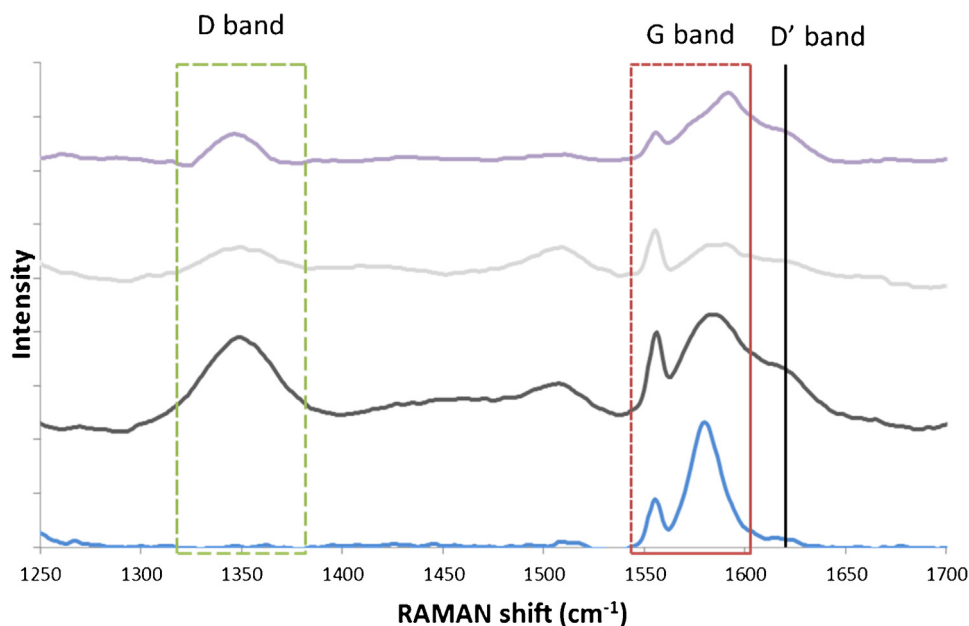
Fig. 4. Raman spectrum of the used Fe–Ni sample (DRM for 1 h, 1023 K, CH_4/CO_2 = 1.1, total pressure of 101.3 kPa). Blue line: graphite, black line: used Fe–Ni catalyst, grey line: used Fe–Ni catalyst after CO_2–TPO up to 950 K (removal of shoulder peak on Fig. 3A), purple line: Fe–Ni catalyst after CO_2–TPO up to 1123 K. (For interpretation of the references to color in this figure legend, the reader is referred to the web version of this article.)

firmed the existence of two types of carbon species structures. The G band of single crystal graphene shifted from 1581 cm^{-1} to 1584 cm^{-1} implying the presence of graphitic-like carbon species in the catalyst (more graphene layers). According to literature, the G Raman peak changes in position, shape and intensity as a function of the number of graphene layers [55]. The D and D′ bands at 1350 and 1619 cm^{-1} were also observed and can be attributed to a defective and disordered structure [53,55]. The disordered carbon species structure, following from the D band, can be amorphous. Amorphous and graphitic-like carbon were also observed by Guo et al. [4], who performed Raman spectroscopy over Ni/MgAl$_2$O$_4$ after coking via CH$_4$ temperature programmed decomposition. The Raman spectrum of Fe–Ni after CO$_2$–TPO at 950 K (grey line in Fig. 4) showed the same peaks as the used Fe–Ni catalyst (black line in Fig. 4) that was not treated by oxidation, implying the existence of the same types of carbon. This enhances the aforementioned statement that the shoulder peak in the CO$_2$–TPO profile of used Fe–Ni (Fig. 3A) is ascribed to carbon species oxidation by Ni surface oxygen, originating from CO$_2$ dissociation. Finally, the same type of carbon is observed on the Fe–Ni catalyst after CO$_2$ treatment at 1123 K, implying that only carbon close to active metals can be oxidized by CO$_2$. This is in agreement with the XRD full scan patterns (Fig. 1) and EDX element mapping of Fe–Ni (Fig. 2) where carbon was still observed after CO$_2$ oxidation.

Fig. 5(A) shows a TEM image of a used Fe–Ni catalyst. The presence of filamentous carbon with Fe–Ni alloy particles on top is observed, which can be verified by the EDX mapping (Fig. 5(B–D)).

XPS was performed on the material in two different states: reduced and used Fe–Ni. The XPS wide scans showed photoemission lines for C, O, Mg, Al, Ni and Fe. The surface concentrations of Ni and Fe in the fresh sample amounted to 4.5 and 1.0 at%, respectively. The wide scan after reaction in CH$_4$:CO$_2$ with 1:1 ratio stood out as its survey was dominated by a very strong C1s intensity. Next to this photoemission peak, only O1s was detected, while other elements were not observable. The latter evidenced the presence of a large amount of C at the surface, covering all of the catalyst surface with considerable thickness, thereby suppressing photoelectron signals from other surface elements.
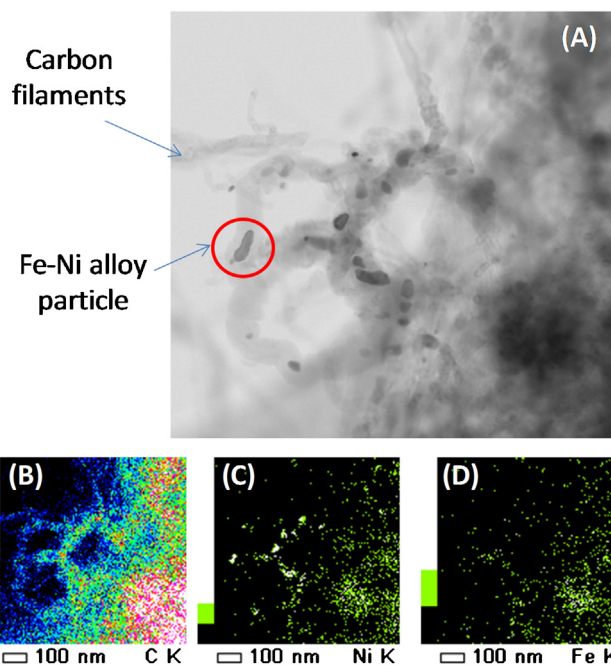
Fig. 5. (A) HRTEM image of a used Fe–Ni catalyst (after DRM at 1023 K, CH$_4$/CO$_2$/He = 1.1/1/1, total pressure of 101.3 kPa, reaction time 1 h). EDX element mapping of (B) carbon, (C) Ni and (D) Fe.

Fig. 6 shows the C1s photoemission signal for these two states of the material, calibrated to 284.6 eV. For the reduced state, a shoulder is apparent at binding energy 288.3 eV, next to the main C intensity. This C1s signal is representative of adventitious carbon contamination and consists of a main component at 284.6 eV for CC bonds, and smaller contributions at 286 eV for O—C and 288.3 eV for C=O.

The C1s signal after reaction with CH$_4$:CO$_2$ in a 1:1 ratio differs substantially. First, the main C1s contribution is much more intense than in the previously discussed state. Secondly, it is asymmetric to
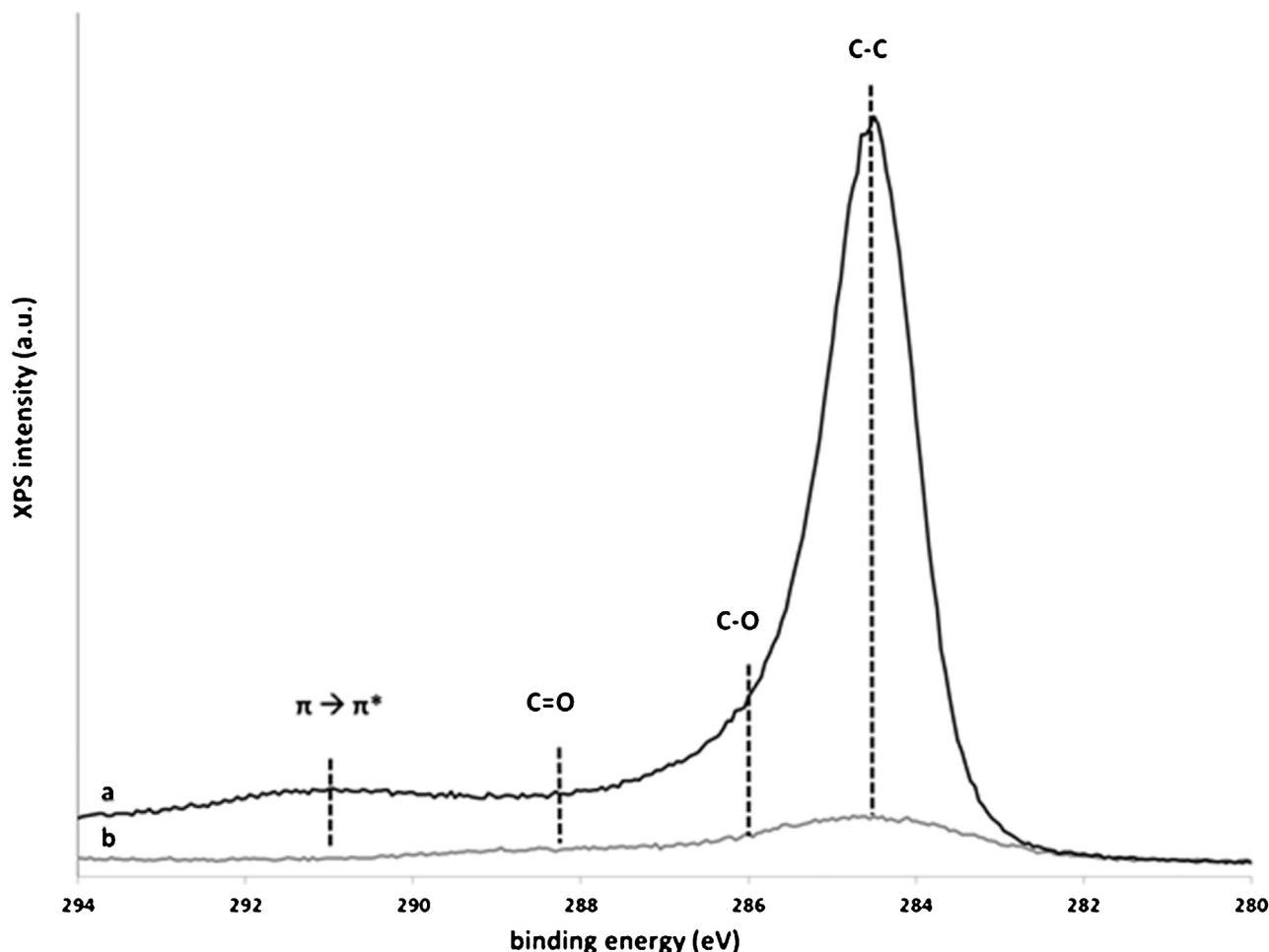
Fig. 6. XPS detail windows of the C1s photoline for Fe–Ni: (a) reduced (b) after DRM reaction in $CH_4/CO_2/He = 1/1/1$.

higher binding energy and has an extra feature at 291 eV. Such C1s photoline is consistent with graphite or graphitic compounds with shake-up satellite ∼6 eV higher in binding energy due to $\pi \rightarrow \pi^*$ transitions [56,57].

Summarizing, the existence of two types of carbon species, amorphous and graphitic-like i.e., filaments, can be concluded from both Raman spectroscopy, HRTEM and XPS. Nickel and iron carbide were not detected from XPS which is in agreement with Fig. 1 where no carbide diffraction peaks were observed during XRD full scans. However, Galvita at al. [23] observed Fe_3C formation during CH_4 reduction of Ni/CeO_2–Fe_2O_3. During DRM Fe partially segregates from Fe–Ni alloy, forming FeO_x due to CO_2 presence. The FeO_x formation removes carbon species as these are oxidized by FeO_x lattice oxygen producing CO. Hence, it is likely that most of the carbon species will be formed during dry reforming on the Ni surface [22].

3.4. Mechanism of carbon removal by CO_2

An operando experiment was performed over used Fe–Ni during CO_2–TPO coupling in situ time resolved XRD with MS. In situ XRD (Fig. 7(A)) showed that during oxidation, the Fe–Ni alloy peak (43.7–44.2°) shifted to higher 2θ values (∼44.5°) corresponding to metallic Ni. In addition, two peaks at diffraction areas 35.4–36.4° and 42.8–43.5° appeared implying the formation of Fe_3O_4. This is in agreement with previous results [22] where Fe–Ni alloy was found to decompose during CO_2 oxidation yielding two separate phases of Ni and Fe_3O_4. The intensity of the graphite diffraction in the angular region 25.8–26.8° decreased at 1050 K because of its removal

by CO_2. However, Fig. 7(A) shows that graphite was not completely removed by CO_2 which is in agreement with Fig. 2(B) where carbon species were still observed on the support after CO_2–TPO. Fig. 7(B) shows the CO intensity variation with temperature obtained by MS corresponding to CO produced by carbon species removal. Another operando CO_2–TPO experiment (not shown) over reduced Fe–Ni catalyst was performed in order to separate the CO production originating from Fe oxidation and from carbon species removal by CO_2. No CO intensity was detected by MS because of low CO concentration whereas Fe_3O_4 formation was observed in the 2D in situ XRD patterns. This implies that CO intensity during the operando CO_2–TPO over the used Fe–Ni catalyst (Fig. 7(B)) corresponds to carbon species removal by CO_2. The kinetics of alloy decomposition and graphite oxidation are illustrated in Fig. 7(C) as time-dependent integral intensities of the Fe–Ni alloy, Ni, Fe_3O_4 and graphite angular regions.

The intensity of characteristic peaks associated with crystalline $MgAl_2O_4$ did not change throughout CO_2–TPO up to the final temperature of 1123 K. The small shift of angular positions compared to full scan XRD patterns at room temperature can be ascribed to temperature-induced lattice expansion and different sample height. The peak maximum of CO in Fig. 7(B) at 1050 K is in agreement with the temperature at which the graphite peak intensity (25.8–26.8°) decreases in Fig. 7(C). The formation of Fe_3O_4 was observed only at 1050 K (Fig. 7(C)), i.e., the same temperature at which the graphite diffraction peak was removed, while it was expected to happen at lower temperature. Fig. 8(A) shows a selected angular region of 35–40° from Fig. 7(A), for used Fe–Ni,
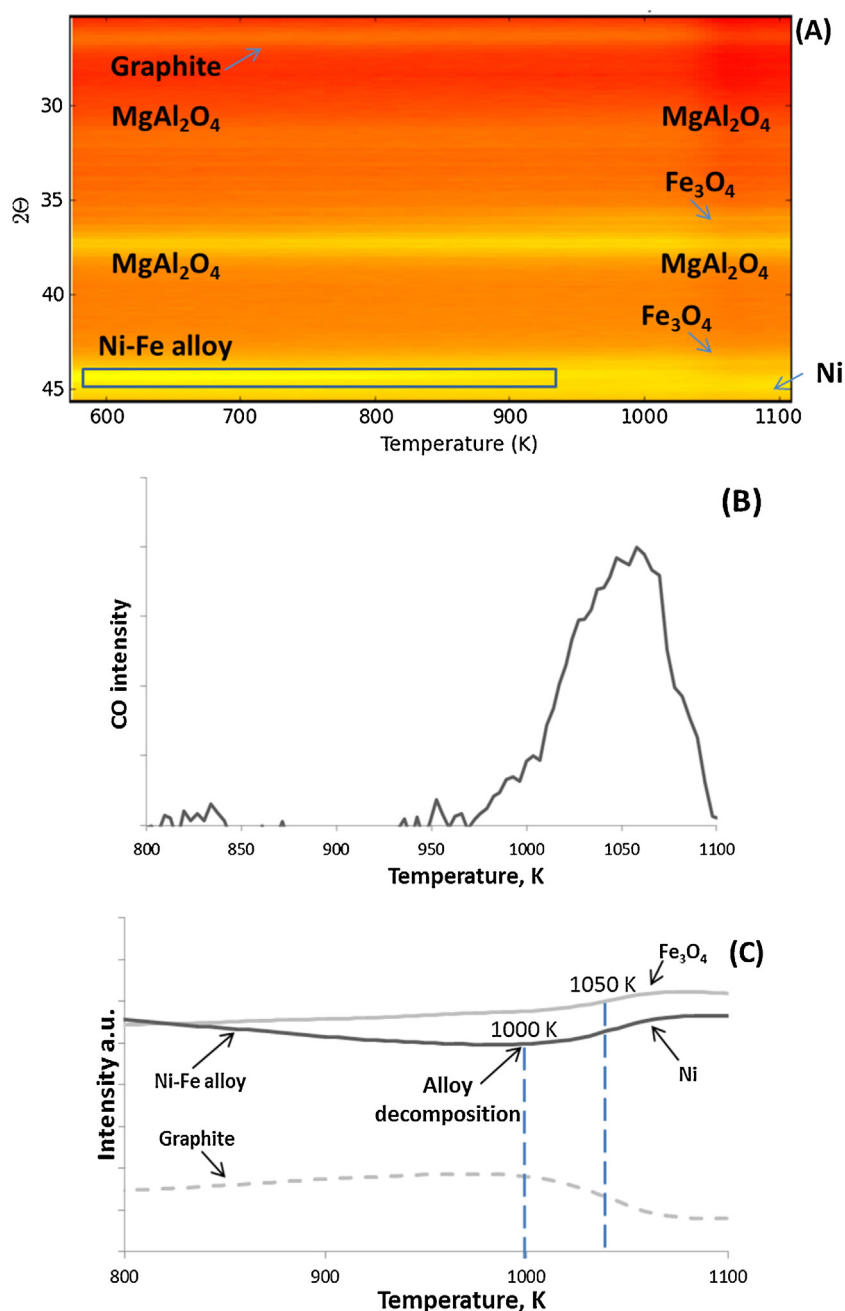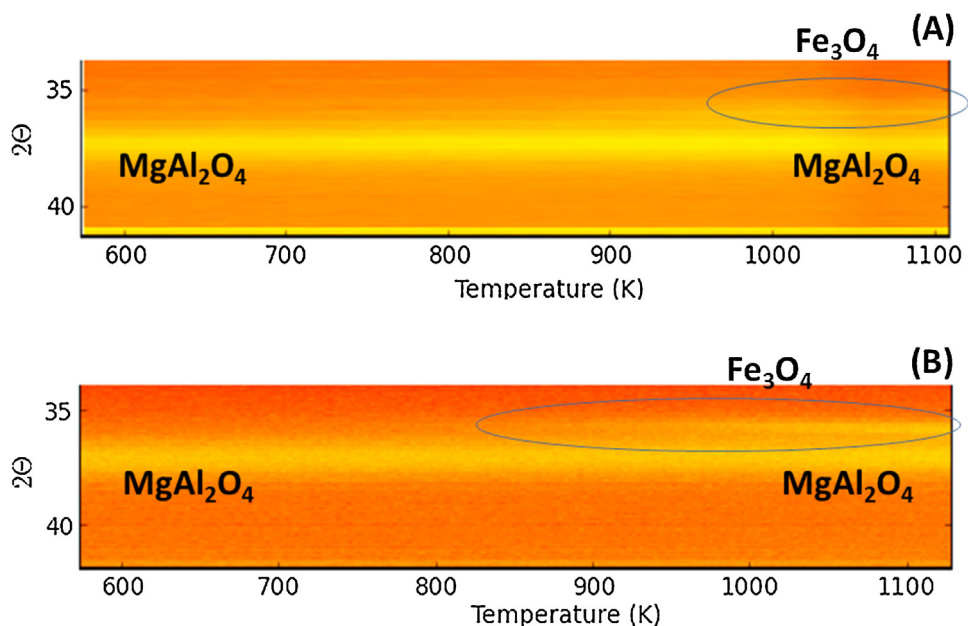
Fig. 7. In situ XRD coupled with MS during CO_2–TPO (heating rate 20 K/min, maximum temperature 1123 K, flow rate 10 ml/s) of used Fe–Ni catalyst (DRM for 1 h, 1023 K, $CH_4/CO_2/He = 1.1/1/1$, total pressure of 101.3 kPa): (A) 2D XRD pattern; (B) CO produced during carbon species removal as a function of temperature; (C) integral intensity variation of (A) for diffraction areas 25.8–26.8° (graphite), 35.4–36.4° (Fe_3O_4) and 43.7–44.2° (Fe–Ni alloy).

where the most intense peak of Fe_3O_4 (35.5°) is located. Fig. 8(B) shows the results obtained by in situ XRD for the same selected angular region (35–40°) during CO_2–TPO of the reduced Fe–Ni catalyst. The start of Fe_3O_4 formation during CO_2–TPO of the used Fe–Ni catalyst is detected at higher temperature, 1050 K, than the 850 K, for CO_2–TPO of the reduced catalyst. This is in agreement with Galvita et al. [58], who performed CO_2–TPO over reduced Ni/CeO$_2$–Fe$_2$O$_3$ and reported reoxidation of Fe–Fe$_3$O$_4$ at 750 K. It implies that in case of CO_2–TPO of used catalyst two reactions occur involving Fe, namely oxidation of Fe by CO_2 and reduction of FeO$_x$ by carbon species respectively, up to 1050 K. At this temperature Fe_3O_4 is formed because the carbon species that were in contact with the catalyst particles have been removed.

The results obtained from the operando XRD experiment are consistent with a mechanism consisting of two parallel processes: (1) dissociation of CO_2 over Ni followed by the oxidation of carbon species by surface oxygen; (2) Fe oxidation by CO_2 and subsequent carbon species oxidation by Fe oxide lattice oxygen (Fe oxide reduction step). In contrast, CO_2 does not interact directly from gas phase with carbon species that are located far from the active sites.

A graphical illustration of carbon species removal over the Fe–Ni catalyst is depicted in Fig. 9. In the latter, the carbon representation is schematic and does not reflect the real structure as determined from the carbon characterization section (see Section 3.3).

Fig. 8. 2D in situ XRD pattern during CO_2–TPO (heating rate 20 K/min, maximum temperature 1123 K, flow rate 10 ml/s). (A) Used Fe–Ni catalyst (DRM for 1 h, 1023 K, CH_4/CO_2 = 1.1, total pressure of 101.3 kPa). Selected angular region of 35–40° from Fig. 7(A). (B) Reduced Fe–Ni catalyst (heating rate: 30 K/min, maximum temperature 1123 K, flow rate: 1 ml/s, 10% H_2/He). Selected angular region of 35–40°.

3.5. In situ time resolved XRD during O_2–TPO

To examine the differences in mechanism between carbon species oxidation by CO_2 and O_2, an O_2–TPO experiment over used Fe–Ni by means of in situ XRD was performed (Fig. 10). During oxidation the Fe-Ni alloy peak (43.7–44.2°) shifted to lower 2θ values (~43.4°) corresponding to NiO (Fig. 10(A)). In addition, a peak in diffraction region 35.7–36.4° appeared implying the formation of Fe_2O_3. The graphite diffraction intensity of 25.8–26.8° disappeared at 950 K because of its oxidation by O_2. This is in agreement with Fig. 3(B) where it was shown that during O_2–TPO, carbon species were completely burnt at 960 K. In contrast to CO_2 oxidation (Fig. 7(A)), where graphite was not completely removed by CO_2, O_2 can oxidize graphite completely at lower temperature. The kinetics of alloy decomposition and graphite oxidation are illustrated in Fig. 10(B) as time-dependent integral intensities of the graphite, Fe–Ni alloy and Fe_2O_3 angular regions.

The mechanism of carbon species gasification during O_2–TPO is different than carbon species removal during CO_2–TPO (Fig. 10). Fe starts to segregate from the Fe–Ni alloy at 780 K, while the decomposition is complete at 850 K and thereafter the graphite oxidation starts. The carbon species oxidation could be ascribed to several processes: lattice oxygen transfer from nickel and iron oxides, oxy-

gen spillover originating from O_2 dissociation, particle migration to carbon that is deposited far from active metals and direct interaction of gas phase O_2 with the carbon. The oxidation of Fe and Ni to Fe_2O_3 and NiO, respectively, was only observed in XRD when graphite was completely removed.

3.6. O_2–TPO over different catalyst bed configurations

To further investigate the contribution of oxygen spillover mechanism to the carbon gasification process another experiment was performed involving O_2– and CO_2– TPO over three different catalyst bed configurations: a mechanical mixture of graphite and Fe–Ni catalyst, a two and a three layers catalyst bed. A CO_2–TPO of all three aforementioned catalyst bed configurations showed no CO production up to 1173 K (not shown) implying that the carbon species which are located far from the active metals cannot be removed by CO_2. Fig. 11(A) displays the CO_2 intensity as a function of temperature during O_2–TPO of the mechanical mixture and pure graphite. The maximum of CO_2 production for the case of the mechanical mixture is shifted to lower temperature (920 K) than for pure graphite (1100 K). Complete oxidation of the graphite content of the mechanical mixture is observed at 1040 K. Compared to the mechanical mixture, graphite oxidation from the
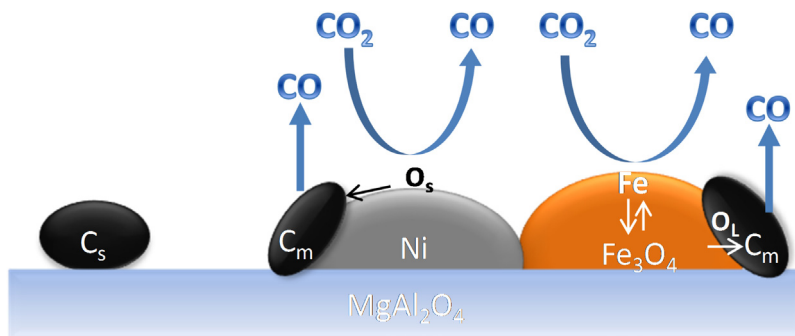
Fig. 9. Schematic representation of carbon species removal by CO_2 over Fe–Ni catalyst. C_s: deposited carbon. O_s: surface oxygen, O_L: lattice oxygen. C_m: carbon deposited on metals, C_s: carbon deposited far from metals, O_s: surface oxygen, O_L: lattice oxygen. The carbon illustration is not corresponding to the real carbon structure.
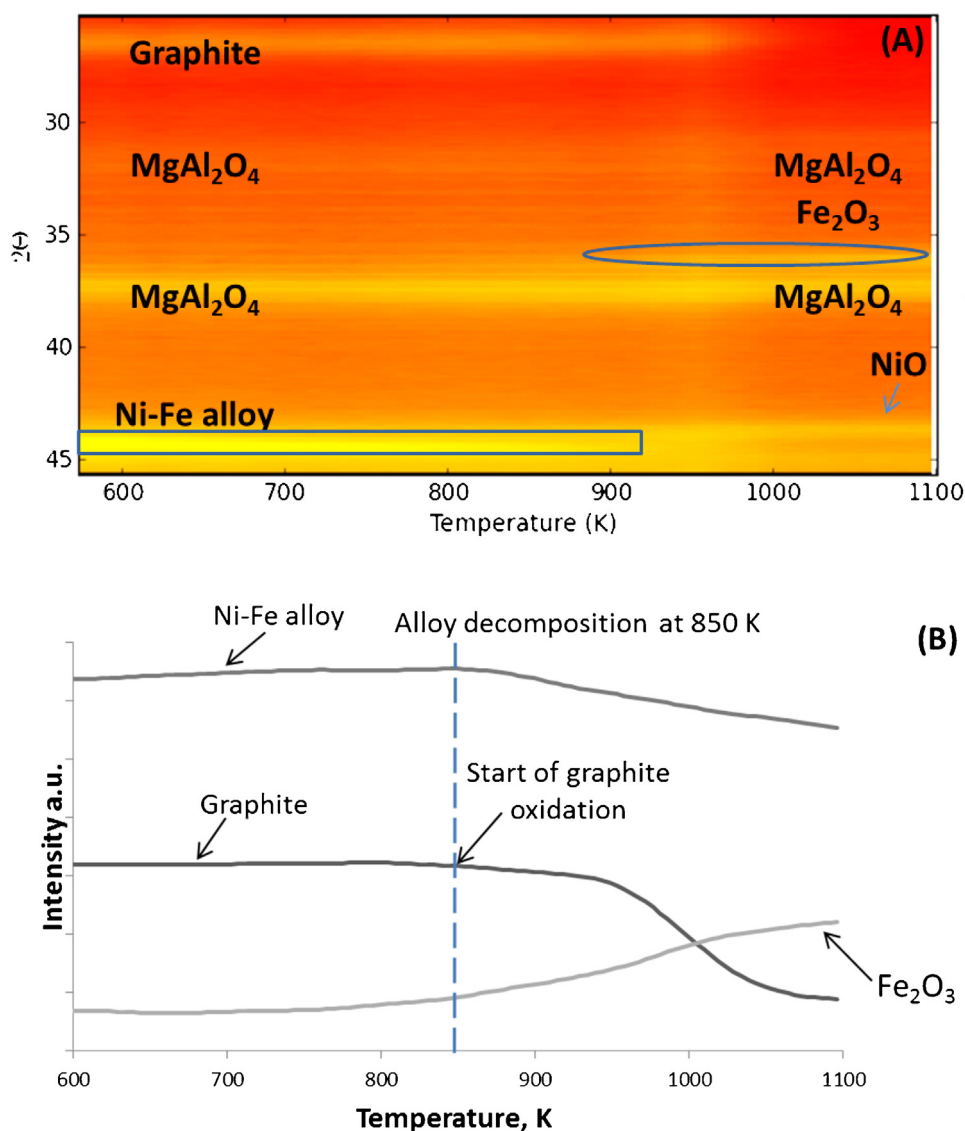
Fig. 10. In situ XRD during O_2–TPO of a used Fe–Ni catalyst (DRM for 1 h, 1023 K, CH_4/CO_2 = 1.1, total pressure of 101.3 kPa). (A) 2D XRD pattern for Fe–Ni. Heating rate: 20 K/min, maximum temperature 1123 K, flow rate: 10 ml/s, air. (B) Integral intensity variation of (A) for diffraction areas 25.8–26.8° (graphite), 35.7–36.4° (Fe_2O_3) and 43.7–44.2° (Fe–Ni alloy).

used Fe–Ni sample occurred at close to the same temperature (see Fig. 10(B)) implying that in carbon oxidation behavior, the used catalyst resembles a mechanical mixture of Fe–Ni catalyst and graphite.
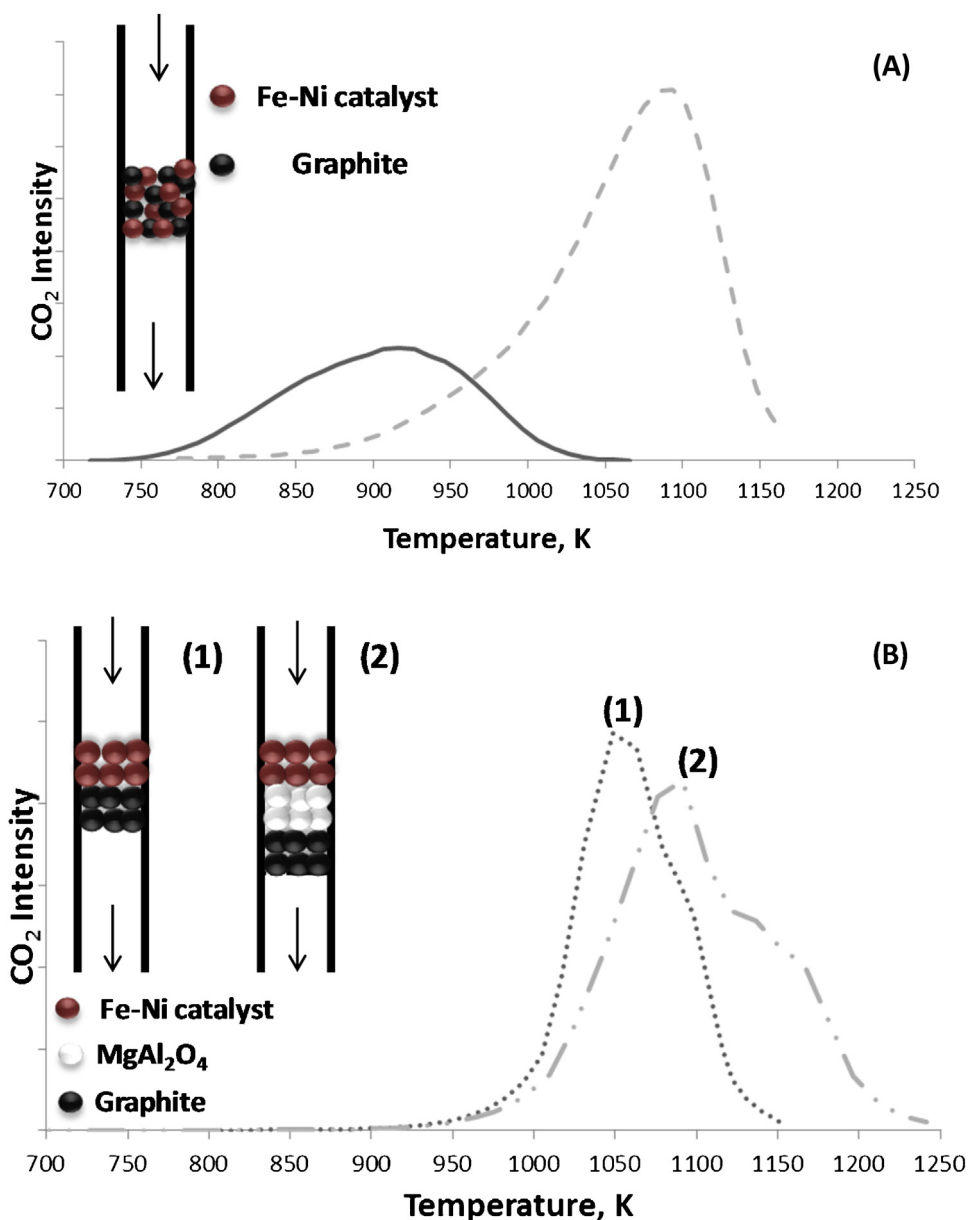
O_2–TPO was also performed over a two- and three-layers catalyst bed (Fig. 11(B)). The two-layers catalyst bed included one layer of Fe–Ni catalyst and one layer of graphite (dot-line) while the three-layers catalyst bed included Fe–Ni catalyst, $MgAl_2O_4$ and graphite (dash-dot dot line). The peak maximum during O_2–TPO over the two-layers reactor bed occurred at lower temperature (1030 K) compared to the three-layers reactor bed (1100 K). This was attributed to the fact that there was contact at the interface between the catalyst and graphite, allowing graphite oxidation through lattice oxygen of nickel and iron oxides.

The peak maximum during O_2–TPO over the three-layers bed lies at the same temperature as for pure graphite (1100 K) indicating that oxygen surface species do not migrate through the layer of $MgAl_2O_4$ in between Fe–Ni catalyst and graphite. Therefore, there is no evidence of oxygen spillover to graphite and its contribution to the carbon gasification process is considered negligible. Further-

more, the better the contact between the catalyst and the carbon, the lower the temperature for carbon oxidation (Fig. 11).

3.7. Temporal analysis of products (TAP) experiments

TAP reactor experiments were applied in order to investigate the isothermal carbon gasification process by CO_2 and O_2 at 993 K. As a first step, the catalyst was aged by a sequence of 400CH_4 pulses. Then, pulses of the oxidizing gas (CO_2 or O_2) were admitted to the reactor. Fig. 12 shows the 2D view of CO_2 responses as a function of pulse number over Ni and Fe–Ni. No CO formation was observed during O_2 pulses. Changing of color from blue to dark red corresponds to an increase in CO_2 produced during pulsing. Fig. 12(A) showed a gradual intensity increase of the CO_2 response during the first five pulses, while shifting the peak maximum to higher times. In order to visualize the individual response peak shapes, Fig. 12(B) displays CO_2 responses after the 1st, 4th and 7th O_2 pulse over aged Ni. After the 1st pulse, the CO_2 peak maximum grew into a sharp peak located around time equal to 0.5 s, while at the 7th pulse a more broad peak is located at 6 s. Throughout

Fig. 11. O_2–TPO profile: CO_2 intensity as a function of temperature for (A) mechanical mixture of graphite and Fe–Ni catalyst (solid line) and for graphite only (dashed line), (B): two and three layers catalyst bed configuration, including one layer of Fe–Ni catalyst and one layer of graphite (dot line) and a Fe–Ni catalyst, $MgAl_2O_4$ support and graphite (dash-dot dot line), respectively. Heating rate of 10 K/min, flow rate of 1 ml/s of 10% O_2/He.

these pulses, conversion of O_2 was 100% (see Fig. S1). The low CO_2 response intensity at the start of the TAP experiment thus indicates O_2 is being consumed in a process, adsorption or metal oxidation, other than carbon gasification. The gradual increase in CO_2 intensity then shows gasification is becoming more important. The peak maximum shift on the other hand, points to an additional process of carbon gasification, requiring more time for CO_2 to appear. Most of the carbon is burnt-off after the 7th O_2 pulse. For aged Fe–Ni, the onset of CO_2 response is longer compared to Ni (Fig. 12(C)). The CO_2 intensity steadily increased and shifted to higher peak maximum times from 0.1 s for pulse 1, 0.7 s at pulse 15–1.2 s for the 29th pulse, further to 1.8 s at the 40th and back to 0.12 s at the 50th pulse. Up to the 45th pulse, the O_2 conversion remained at 100% (see Fig. S1). Qualitatively similar results were obtained for carbon gasification by O_2 pulses at lower temperatures of 873 K and 923 K, which can

be ascribed to the strong exothermicity of the carbon gasification reaction, yielding an increase in the local temperature.

The onset in CO_2 response intensity observed for both Ni and Fe–Ni catalysts implies that the initial O_2 pulses are not involved in carbon gasification. From XRD during O_2–TPO (Fig. 10) it was observed that alloy decomposition and metal oxidation took place before graphite's burn-off. Hence, from the present TAP experiments it is concluded that metals oxidation occurred first and only thereafter the carbon gasification process started.

The shift in time of the CO_2 peak maximum indicates a change in process of CO_2 formation. Possible processes are: (a) oxygen spillover from the active metals to carbon on the support, (b) migration of active particles towards deposited carbon, (c) carbon bulk diffusion through the metal particle to the region where the gasification reaction takes place.
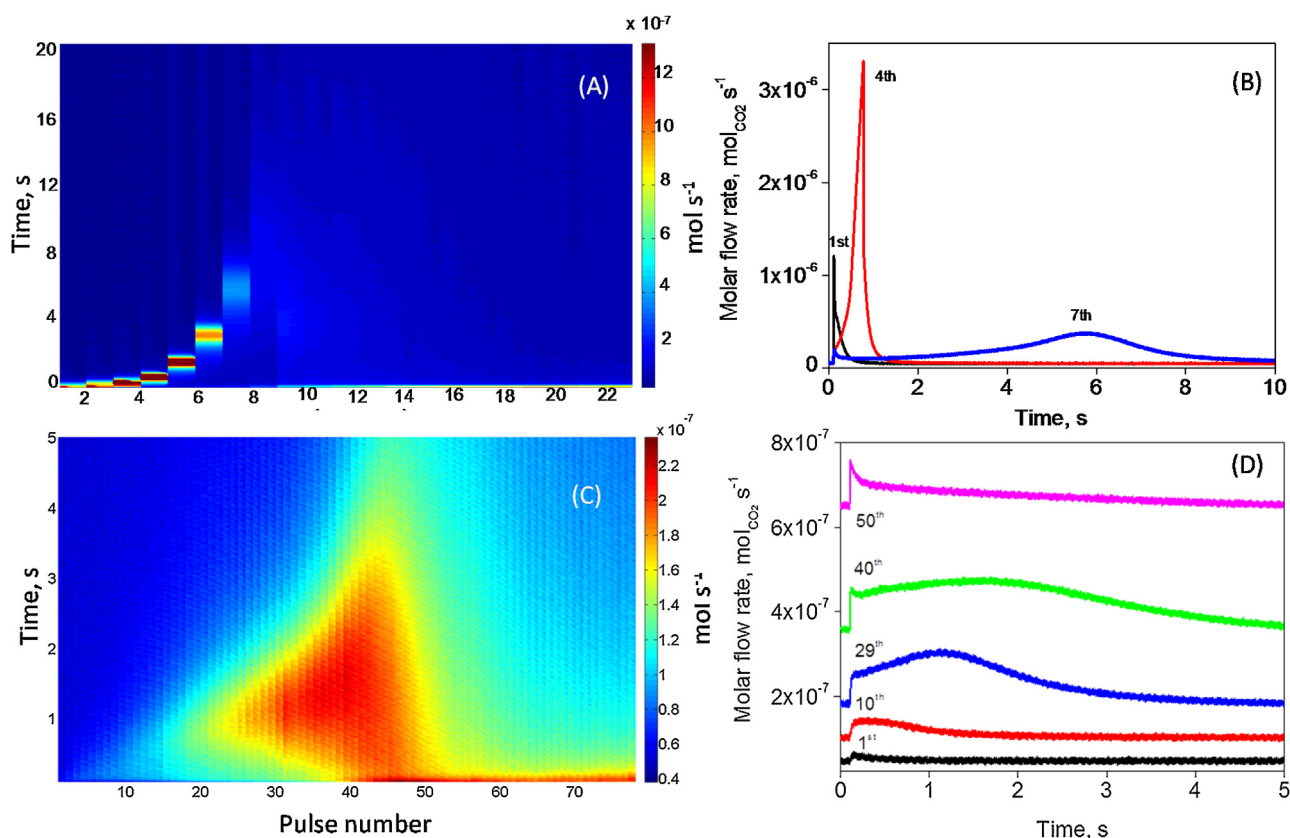
Fig. 12. CO_2 response during O_2 pulses at TAP reactor at 993 K. (A) 2D view for Ni, (B) CO_2 molar flow rate produced during selected O_2 pulses over Ni, (C) 2D view for Fe–Ni, (D) CO_2 molar flow rate produced during selected O_2 pulses over Fe–Ni. Ni and Fe–Ni aged by a sequence of 400CH$_4$ pulses.

The observed time shift is related to surface transport, implying a diffusion process. The diffusion coefficient can be assessed by applying the Einstein approximation equation (Eq. (5)):

$$D = \frac{x^2}{t} \tag{5}$$

where x is the mean traveled distance of the species (m) and D is the diffusion coefficient (m^2 s^{-1}). The characteristic distance, which needs to be bridged by species to reach reactive sites can be estimated from TEM of a TAP aged catalyst (Fig. 13) and is approximately equal to 8–10 nm. This distance can either apply to O spillover, moving from the active metal to the edge of the carbon deposit, to carbon transfer from the edge towards the active metal, or to metal transfer. For carbon gasification by O_2 over the catalysts at 993 K, the diffusion coefficient calculated according to Eq. (5) was approximately 10^{-17} m^2 s^{-1}.

Oxygen spillover provides active oxygen species on the metal surface, which then transfer towards carbon over the support. For such oxygen, the surface diffusion coefficient on MgO amounts to approximately 10^{-16} m^2 s^{-1}, i.e., close to the calculated value [59]. To further evaluate oxygen spillover as possible process, another TAP experiment of O_2 pulses was performed over an oxidized Fe–Ni catalyst (not shown). The O_2 peak that was measured in the outlet of the reactor was sharp and short in time, 0.3 s while the amount of O_2 that was measured in the outlet corresponded to 95% of the inlet pulse, implying the formation of a negligible amount of surface oxygen. This observation enhances the conclusion that was made about the negligible contribution of oxygen spillover mechanism to the carbon gasification process (see Section 3.6).

The mobility of metal particles on graphite under O_2 and CO_2 was evidenced in 1964 [60]. McKee showed mobility of catalytic particles with channeling on graphite by hot stage optical
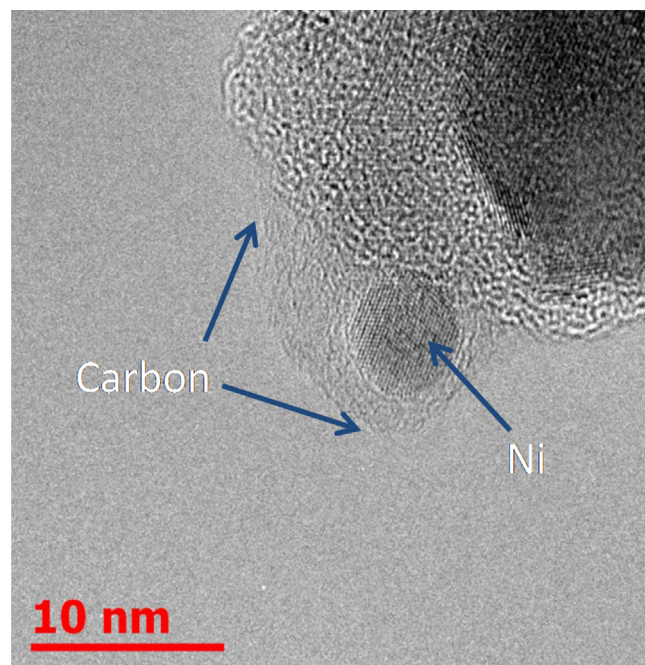
Fig. 13. HRTEM image of aged Ni catalyst after 400CH$_4$ pulses in TAP.

microscopy [61]. Recently, the Environmental TEM (ETEM) technology was applied for in situ imaging during the carbon oxidation process on transition metal particles. Booth et al. [62] and Gardini et al. [63] have demonstrated that such particles may engage in transport through the layers of carbon deposits during carbon
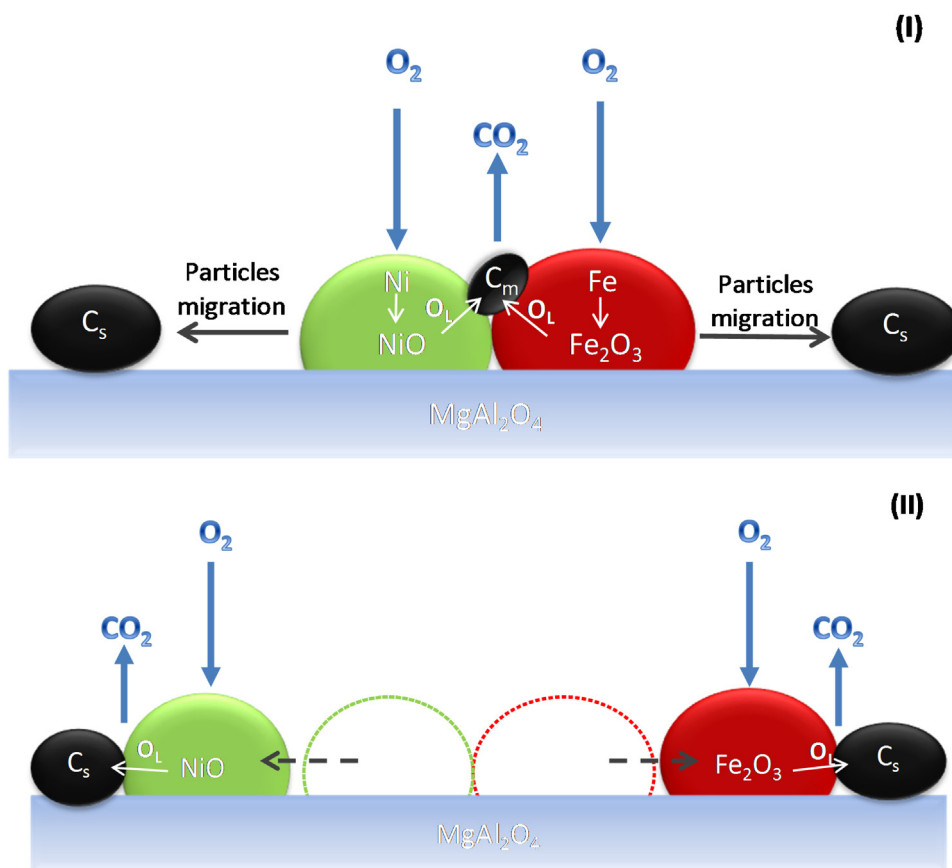
Fig. 14. Schematic representation of carbon species oxidation by O_2 over Fe–Ni catalyst. Two different mechanisms are illustrated: (I) carbon gasification on the active metal (II) particles migration followed by carbon gasification through lattice oxygen. C_m: carbon deposited on metals, C_s: carbon deposited far from metals, O_s: surface oxygen, O_L: lattice oxygen. The carbon illustration does not represent the actual carbon structure.

gasification by O_2. The mobility temperature of various metal and metal oxide particles dispersed on graphite was investigated by Baker [64]. For 10 nm particle size of several metals and oxides, he found that the mobility temperature coincided with the Tammann temperature of these materials, which was expressed as 0.52*Bulk melting point(K). In case of NiO and Fe_2O_3, the Tammann temperature is equal to 1290 K and 1080 K, respectively, close to the temperature at which the TAP experiments were performed (993 K).

Carbon gasification by O_2 is an exothermic process ($\Delta H = -390$ kJ/mol), which will result in a local temperature increase. Gasification occurring on the active metal surface will make the metal particle hotter than its surroundings, which will increase its mobility and hence allow it to migrate. Hence, carbon species which are located away from the metal particles can still be oxidized after the latter migrate.

As for carbon transfer, it is well documented that the diffusion coefficient of carbon inside of Ni or Fe is equal to approximately 10^{-13} m^2 s^{-1} [65] which value is significant higher, implying that it is a faster process than the calculated value. Hence, carbon transfer cannot account for the time shifts observed.

The above isothermal TAP experiments were repeated with CO_2 pulses for carbon oxidation. CO was monitored as a carbon gasification product. No onset occurred for either catalyst, and the responses were all narrow and remained stable in time position. The amount of CO produced gradually decreased with pulse number as carbon was removed from the surface (see Fig. S2). Subsequent pulses of O_2 however gave more CO_2 response, indicating that not all carbon was gasified by CO_2.

3.8. Carbon gasification mechanism by O_2

Based on above-mentioned results from different techniques, a concluding mechanism for O_2 mediated carbon gasification is proposed. The oxidation of carbon species by O_2 can be described as follows: (1) oxidation of metal particles Ni and Fe; (2) surface carbon gasification through lattice oxygen, from the active metal oxides, (3) particle migration to the contact points between catalyst and carbon species, enhanced by high local temperature arising from (2) and (4) subsequent oxidation of distant carbon through lattice oxygen of nickel and iron oxides. The effect of oxygen spillover to the support towards distant carbon is considered to be negligible.

A graphical illustration of the O_2 carbon species oxidation over Fe–Ni catalyst is depicted in Fig. 14, including the contribution for local and distant carbon gasification. During O_2 oxidation, Fe_2O_3 and NiO are formed before carbon species oxidation, as it was concluded from TAP experiments (Fig. 12). Fig. 14(I) shows the local carbon gasification process over the Fe–Ni catalyst. Fig. 14(II) illustrates the mechanism of particles diffusion to carbon species that are located far from the active metals [62,63]. Their migration is made possible due to the local temperature increase, originating from surface carbon oxidation. Then, the distant carbon species are oxidized through the lattice oxygen of the nickel and iron oxides. Alternatively, the mechanism of carbon bulk diffusion through the metal particles, resulting in dissolved carbon, introduced by Figueiredo and Trimm [29], cannot be excluded. However, our observation is that initially metal oxides are formed and afterwards the carbon gasification process starts.

4. Conclusions

Carbon removal is examined from 8 wt% Ni-5 wt% Fe catalysts on a MgAl$_2$O$_4$ support after methane dry reforming at 1023 K atmospheric pressure and a CH$_4$/CO$_2$ ratio of 1:1. The existence of two different carbon species structures, graphitic and amorphous, was determined by Raman spectroscopy, XPS and TEM.

CO$_2$-regeneration resulted in the removal of carbon on the active metals of the catalysts. However, EDX-STEM mapping showed the persistence of carbon species located far from the catalyst active metals, implying the absence of direct interaction between carbon species and CO$_2$ from the gas phase.

Operando XRD and isothermal TAP experiments allowed to identify the major mechanistic aspects of carbon species removal by CO$_2$ over used Fe–Ni catalyst. The process could be described by two parallel contributions. One contains the dissociation of CO$_2$ over Ni and subsequent oxidation of carbon species by the surface oxygen. The second consists of the Fe oxidation by CO$_2$ followed by carbon species oxidation by Fe oxide lattice oxygen, i.e., Fe oxide reduction.

The mechanism of carbon species oxidation by O$_2$ was examined using time-resolved in situ XRD, TPO of different catalyst bed configurations and isothermal TAP experiments. The gasification of carbon species can be described by two processes: (1) oxidation of surface carbon and (2) particles migration to the carbon species that are deposited far from active metals and subsequent oxidation through lattice oxygen of the iron and/or nickel oxides. The contribution of oxygen spillover in carbon gasification was considered to be negligible.

Acknowledgments

Appendix A. Supplementary data

Supplementary data associated with this article can be found, in the online version, at http://dx.doi.org/10.1016/j.apcatb.2015.12.006.

References

[1] L. Guczi, G. Stefler, O. Geszti, I. Sajó, Z. Pászti, A. Tompos, Z. Schay, Appl. Catal. A 375 (2010) 236–246.
[2] D. Pakhare, V. Schwartz, V. Abdelsayed, D. Haynes, D. Shekhawat, J. Poston, J. Spivey, J. Catal. 316 (2014) 78–92.
[3] I. Luisetto, S. Tuti, E. Di Bartolomeo, Int. J. Hydrogen Energy 37 (2012) 15992–15999.
[4] J. Guo, H. Lou, X. Zheng, Carbon 45 (2007) 1314–1321.
[5] L.S. Lobo, Carbon Formation from Hydrocarbons on Metals, Department of Chemical Engineering and Chemical Technology, Imperial College of Science and Technology, 1971.
[6] L.S. Lobo, J.L. Figueiredo, C.A. Bernardo, Catal. Today 178 (2011) 110–116.
[7] L.S. Lobo, D.L. Trimm, Nat. Phys. Sci. 234 (1971) 15–16.
[8] S. Damyanova, B. Pawelec, K. Arishtirova, J.L.G. Fierro, Int. J. Hydrogen Energy 37 (2012) 15966–15975.
[9] C.H. Bartholomew, Appl. Catal. A: Gen. 212 (2001) 17–60.
[10] T.H. Gardner, J.J. Spivey, E.L. Kugler, D. Pakhare, Appl. Catal. A 455 (2013) 129–136.
[11] D. Pakhare, J. Spivey, Chem. Soc. Rev. 43 (2014) 7813–7837.
[12] A. Horváth, G. Stefler, O. Geszti, A. Kienneman, A. Pietraszek, L. Guczi, Catal. Today 169 (2011) 102–111.
[13] C.E. Daza, S. Moreno, R. Molina, Int. J. Hydrogen Energy 36 (2011) 3886–3894.
[14] J.R. Rostrupnielsen, J.H.B. Hansen, J. Catal. 144 (1993) 38–49.
[15] A. Penkova, L. Bobadilla, S. Ivanova, M.I. Domínguez, F. Romero-Sarria, A.C. Roger, M.A. Centeno, J.A. Odriozola, Appl. Catal. A 392 (2011) 184–191.
[16] Z. Zhang, X.E. Verykios, Appl. Catal. A 138 (1996) 109–133.
[17] A.S. Bobin, V.A. Sadykov, V.A. Rogov, N.V. Mezentseva, G.M. Alikina, E.M. Sadovskaya, T.S. Glazneva, N.N. Sazonova, M.Y. Smirnova, S.A. Veniaminov, C. Mirodatos, V. Galvita, G.B. Marin, Top. Catal. 56 (2013) 958–968.
[18] A. Kambolis, H. Matralis, A. Trovarelli, C. Papadopoulou, Appl. Catal. A 377 (2010) 16–26.
[19] V.V. Galvita, H. Poelman, V. Bliznuk, C. Detavernier, G.B. Marin, Ind. Eng. Chem. Res. 52 (2013) 8416–8426.
[20] H. Ay, D. Üner, Appl. Catal. B 179 (2015) 128–138.
[21] V. Sadykov, V. Muzykantov, A. Bobin, N. Mezentseva, G. Alikina, N. Sazonova, E. Sadovskaya, L. Gubanova, A. Lukashevich, C. Mirodatos, Catal. Today 157 (2010) 55–60.
[22] S.A. Theofanidis, V.V. Galvita, H. Poelman, G.B. Marin, ACS Catal. 5 (2015) 3028–3039.
[23] V.V. Galvita, H. Poelman, G.B. Marin, J. Power Sources 286 (2015) 362–370.
[24] J. Ashok, S. Kawi, ACS Catal. 4 (2014) 289–301.
[25] L. Wang, D. Li, M. Koike, S. Koso, Y. Nakagawa, Y. Xu, K. Tomishige, Appl. Catal. A 392 (2011) 248–255.
[26] A. Djaidja, H. Messaoudi, D. Kaddeche, A. Barama, Int. J. Hydrogen Energy 40 (2015) 4989–4995.
[27] L.S. Lobo, Appl. Catal. B: Environ. 148–149 (2014) 136–143.
[28] L.S. Lobo, Catal. Rev. 55 (2013) 210–254.
[29] J.L. Figueiredo, D.L. Trimm, J. Catal. 40 (1975) 154–159.
[30] C.A. Bernardo, D.L. Trimm, Carbon 17 (1979) 115–120.
[31] A. Tomita, Y. Tamai, J. Catal. 27 (1972) 293–300.
[32] E. Baumgarten, A. Schuck, Appl. Catal. 37 (1988) 247–257.
[33] F. Kapteijn, J.A. Moulijn, Carbon and Coal Gasification, in: J. Figueiredo, J. Moulijn (Eds.), Springer, The Netherlands, 1986, pp. 291–360.
[34] D. Fino, N. Russo, C. Badini, G. Saracco, V. Specchia, AICHE J. 49 (2003) 2173–2180.
[35] B.R. Stanmore, V. Tschamber, J.F. Brilhac, Fuel 87 (2008) 131–146.
[36] M. Machida, Y. Murata, K. Kishikawa, D. Zhang, K. Ikeue, Chem. Mater. 20 (2008) 4489–4494.
[37] N. Zong, Y. Liu, Thermochim. Acta 527 (2012) 22–26.
[38] W. Gac, A. Denis, T. Borowiecki, L. Kępiński, Appl. Catal. A 357 (2009) 236–243.
[39] A.S.A. Al-Fatish, A.A. Ibrahim, A.H. Fakeeha, M.A. Soliman, M.R.H. Siddiqui, A.E. Abasaeed, Appl. Catal. A 364 (2009) 150–155.
[40] C.A. Querini, S.C. Fung, Catal. Today 37 (1997) 277–283.
[41] K.M. Hardiman, C.G. Cooper, A.A. Adesina, R. Lange, Chem. Eng. Sci. 61 (2006) 2565–2573.
[42] J.M. Kanervo, A.O.I. Krause, J.R. Aittamaa, P.H. Hagelberg, K.J.T. Lipiäinen, I.H. Eilos, J.S. Hiltunen, V.M. Niemi, Chem. Eng. Sci. 56 (2001) 1221–1227.
[43] A. Tomita, Catal. Surv. Jpn. 5 (2001) 17–24.
[44] J.T. Gleaves, G. Yablonsky, X. Zheng, R. Fushimi, P.L. Mills, J. Mol. Catal. A: Chem. 315 (2010) 108–134.
[45] U. Menon, V.V. Galvita, G.B. Marin, J. Catal. 283 (2011) 1–9.
[46] J. Haber, J.H. Block, B. Delmon, Pure Appl. Chem. (1995).
[47] J.J. Carberry, D. White, Ind. Eng. Chem. 61 (1969) 27–35.
[48] G.F. Fromen, K. Bischoff, Chemical Reactor Analysis and Design, John Wiley & Sons, 1990.
[49] D.E. Mears, J. Catal. 20 (1971) 127–131.
[50] R.T.K. Baker, Preprint Pap. Am. Chem. Soc. Div. Fuel Chem. 41 (1996) 521–524.
[51] N. Shah, D. Panjala, G.P. Huffman, Energy Fuels 15 (2001) 1528–1534.
[52] D. Espinat, H. Dexpert, E. Freund, G. Martino, M. Couzi, P. Lespade, F. Cruege, Appl. Catal. 16 (1985) 343–354.
[53] H. Darmstadt, L. Sümmchen, J.M. Ting, U. Roland, S. Kaliaguine, C. Roy, Carbon 35 (1997) 1581–1585.
[54] T. Jawhari, A. Roid, J. Casado, Carbon 33 (1995) 1561–1565.
[55] A.C. Ferrari, Solid State Commun. 143 (2007) 47–57.
[56] H. Estrade-Szwarckopf, Carbon 42 (2004) 1713–1721.
[57] A.V. Shchukarev, D.V. Korolkov, Cent. Eur. J. Chem. 2 (2004) 347–362.
[58] V.V. Galvita, H. Poelman, C. Detavernier, G.B. Marin, Appl. Catal. B 164 (2015) 184–191.
[59] D. Martin, D. Duprez, J. Phys. Chem. 100 (1996) 9429–9438.
[60] J.M. Thomas, P.L. Walker, J. Chem. Phys. 41 (1964) 587–588.
[61] D.W. McKee, Carbon 8 (1970) 131–139.
[62] T.J. Booth, F. Pizzocchero, H. Andersen, T.W. Hansen, J.B. Wagner, J.R. Jinschek, R.E. Dunin-Borkowski, O. Hansen, P. Bøggild, Nano Lett. 11 (2011) 2689–2692.
[63] D. Gardini, J.M. Christensen, C.D. Damsgaard, A.D. Jensen, J.B. Wagner, Appl. Catal. B 183 (2016) 28–36.
[64] R.T.K. Baker, J. Catal. 78 (1982) 473–476.
[65] J.J. Lander, H.E. Kern, A.L. Beach, J. Appl. Phys. 23 (1952) 1305–1309.